

Production of Monodisperse Gold Nanobipyramids with Number Percentages Approaching 100% and Evaluation of Their Plasmonic Properties

Qian Li, Xiaolu Zhuo, Shuang Li, Qifeng Ruan, Qing-Hua Xu, and Jianfang Wang*

Gold nanobipyramids (NBPs) and nanorods (NRs) are two common types of elongated colloidal plasmonic metal nanocrystals, with their longitudinal plasmon wavelengths synthetically tunable over a wide spectral range. Au NBPs have sharper tips and narrower shape and size distributions than Au NRs. However, the number percentages of Au NBPs have been limited below $\approx 60\%$. Herein, a method for producing Au NBPs with number percentages approaching 100% and longitudinal plasmon resonance wavelengths synthetically tuned from ≈ 700 to ≈ 1200 nm is reported. This method relies on a stepwise combination of seed-mediated growth, Ag overgrowth, depletion force-induced self-separation, and final chemical etching of Ag. The obtained Au NBPs have the same shapes and sizes as the directly grown ones. Systematic comparisons of the plasmonic properties between the purified Au NBP and high-yield single-crystalline Au NR samples show unambiguously that Au NBPs are superior to Au NRs in terms of the plasmon peak width, refractive index sensitivity, figure of merit, two-photon photoluminescence, and surface-enhanced Raman scattering.

Despite the excellent plasmonic properties and various applications demonstrated for Au NRs, they still possess several shortcomings. In general, they exhibit relatively large size and shape distributions.^[7–9,13] In particular, their end shapes are highly dependent on the synthetic conditions.^[31] Such distributions cause the longitudinal plasmon peaks of ensemble Au NR samples to be inhomogeneously broadened, with the full width at half maximum (FWHM) values ranging from ≈ 100 to ≈ 200 nm. In addition, the usually rounded end shape of Au NRs gives a relatively small local electric field enhancement, which is unfavorable for plasmon-enhanced spectroscopy. As a result, there is still much room and motivation for making elongated Au nanocrystals with narrower size and shape distributions, smaller plasmon peak widths and stronger local electric field enhancements.

1. Introduction

Gold nanocrystals have been regarded as promising nanomaterials owing to their unique physicochemical and plasmonic properties, and extensively employed in diverse applications ranging from biotechnology,^[1] diagnostics,^[2] nanomedicine,^[3] spectroscopy,^[4] optics,^[5] and solar energy harvesting.^[6] In particular, elongated Au nanocrystals, such as Au nanorods (NRs), have been receiving much attention because of their well-developed synthetic methods, synthetically widely tunable plasmon wavelengths,^[7–10] and absorption/scattering cross-sections,^[7,8,11,12] as well as polarization-sensitive plasmon modes. Such attractive features have made Au NRs favorable for an enormous number of potential applications in areas including biotechnology and nanomedicine,^[13–19] plasmon-enhanced spectroscopy,^[20–25] and optics and optoelectronics.^[26–30]

Besides Au NRs, Au nanobipyramids (NBPs) are another type of elongated Au nanocrystals with tunable longitudinal plasmon resonance wavelengths (LPRWs).^[32–34] A gold NBP is typically composed of two pentagonal pyramids that are connected at their bases, with five equi-angularly separated twinning planes aligned along the length axis.^[35,36] One of the most intriguing properties of Au NBPs is their high monodispersity and therefore suppressed inhomogeneous spectral broadening for the plasmon peaks. The minimization of inhomogeneous damping has allowed for understanding the homogeneous dephasing of Au NBPs^[37] and studying viscoelastic flow phenomena in liquids.^[38] Moreover, Au NBPs are more chemically stable than Au NRs;^[39] they possess higher refractive index sensitivities (RISs) and larger figure of merit (FOM) values than Au NRs;^[31,40,41] their local electric field enhancements are several times larger than those of Au NRs.^[39] Despite these attractive features, the number purities of colloidal Au NBP samples have so far been limited below $\approx 60\%$. The products obtained from seed-mediated growth in the presence of cationic alkylammonium surfactants contain a number of roughly spherical Au nanoparticles.^[35,36,39] There have recently been two reports of Au NBP preparations, where a positively charged polyelectrolyte is used as the stabilizing agent. One is the growth of Au NBPs with large Au decahedrons as seeds,^[42] and the other is the preparation of Au NBPs with the synergistic help of Ag and Pd ions.^[43] Although the products in both preparations are in

Dr. Q. Li, X. L. Zhuo, Q. F. Ruan, Prof. J. F. Wang
Department of Physics
The Chinese University of Hong Kong
Shatin, Hong Kong SAR, China
E-mail: jfwang@phy.cuhk.edu.hk

S. Li, Prof. Q.-H. Xu
Department of Chemistry
National University of Singapore
3 Science Drive 3, Singapore 117543

DOI: 10.1002/adom.201400505



relatively high yields, the Au NBPs in the former display very broad longitudinal plasmon peaks (FWHM values > 150 nm or 300 meV). Those in the latter are not exactly made of two symmetric pentagonal pyramids. They have blunt ends and also broad longitudinal plasmon peaks (FWHM values > 120 nm or 250 meV).

In this work, we report on a method for the production of Au NBPs with their number percentages approaching 100% and their LPRWs synthetically tunable from ≈700 to ≈1200 nm. Our method enables the production of pure colloidal Au NBPs while maintaining the same shape, size and plasmonic properties of Au NBPs as those prepared directly by seed-mediated growth. Moreover, we have performed systematic comparisons of the plasmonic properties between Au NBPs and Au NRs. Our results indicate that Au NBPs generally exhibit better plasmonic properties than Au NRs, including narrower size and shape distributions, smaller FWHM values for the longitudinal plasmon peak, higher RISs and FOM values, stronger two-photon photoluminescence (TPPL), and more pronounced surface-enhanced Raman scattering (SERS) enhancements. We expect that Au NBPs will become a highly desirable nanomaterial for a variety of plasmon-based technological applications.

2. Results and Discussion

2.1. Purification of Au NBPs

The starting Au NBP samples in relatively low number percentages were prepared by seed-mediated growth in aqueous solutions with cetyltrimethylammonium bromide (CTAB) or cetyltributylammonium bromide (CTBAB) as the stabilizing agent.^[35,36,39] The LPRWs of the Au NBP samples were tailored from the visible to near-infrared region by varying the volume ratio between the seed and growth solutions and/or using the surfactants with different head groups. The purification steps of Au NBPs are illustrated schematically in **Figure 1**. The directly grown products contain a large amount of roughly spherical Au nanoparticles. Because the particle volumes of the coexistent spherical Au nanoparticles and Au NBPs in the products are similar, it is difficult to separate Au NBPs out of the products using conventional centrifugation. Although other separation methods for Au nanoparticles with different sizes and/or shapes have been demonstrated, such as asymmetric flow field-flow fractionation,^[44] gel electrophoresis,^[45] density-gradient precipitation and centrifugation,^[46–49] these methods are tedious to be scaled up for processing relatively large quantities of colloidal metal nanoparticles. To address the problem of Au NBP separation, we carried out Ag overgrowth on the directly grown products to obtain bimetallic Au/Ag nanocrystals

by adding AgNO₃ in the presence of cetyltrimethylammonium chloride (CTAC). As shown in our previous study,^[50] Ag overgrowth on the spherical Au nanoparticles and NBPs gave faceted (Au core)@(Ag shell) nanoparticles and Au/Ag heteronanorods, respectively. The preferential Ag overgrowth along the length axis is caused by the penta-twinned crystalline structure of the Au NBPs as well as by the stabilization of the Ag {100} facets with halide ions.^[51,52] The bimetallic product was centrifuged and redispersed into a CTAB solution. The surfactant micelles induced an attractive potential between the Au nanoparticles. This attractive potential is known as depletion interaction.^[53–55] The depletion interaction potential for rod-like particles can be estimated according to^[53]

$$U = -(2a_m)Ld'\Pi_m \quad (1)$$

where the negative sign indicates that the depletion interaction is attractive. In Equation (1), a_m is the radius of the surfactant micelle, L is the length of the particle, d' is the effective edge length, which is dependent on the cross-sectional shape of the rod-like particle, and Π_m is a function of the micelle molar concentration and temperature. Equation (1) indicates that the depletion interaction potential depends on the particle length as well as the micelle concentration. As the Au/Ag heteronanorods grow longer, the depletion interaction between them will become larger. By adjusting the surfactant concentration, the bimetallic heteronanorods preferentially agglomerated together and precipitated gravitationally, while the core@shell nanoparticles remained in the supernatant. The precipitated Au/Ag heteronanorods were collected. The Ag segments were subsequently etched away using a mixture solution of NH₃·H₂O and H₂O₂, resulting in pure Au NBPs. During the etching process, H₂O₂ functioned as the oxidizing agent, and NH₃·H₂O was mainly used to increase the solubility of Ag⁺ through the formation of [Ag(NH₃)₂]⁺ complex ions. The use of H₂O₂ together with NH₃·H₂O was to control the etching strength so that the Ag segments could be etched away completely while the Au NBPs could remain intact. In our experiments, we also examined the depletion-induced self-separation of the Au NBP samples without Ag overgrowth. The separation process was found to be very sensitive to the CTAB concentration. High concentrations of CTAB used to induce separation often led to CTAB crystallization. In addition, this method was unsuitable for purifying small Au NBPs with short LPRWs.

Five Au NBP samples with their LPRWs in the visible and near-infrared regions were prepared and subjected to the purification process. Their LPRWs in aqueous solutions were 690, 833, 914, 1062, and 1155 nm, respectively. The purification results are shown in **Figure 2**. The transmission electron microscopy (TEM) images of the unpurified samples show that

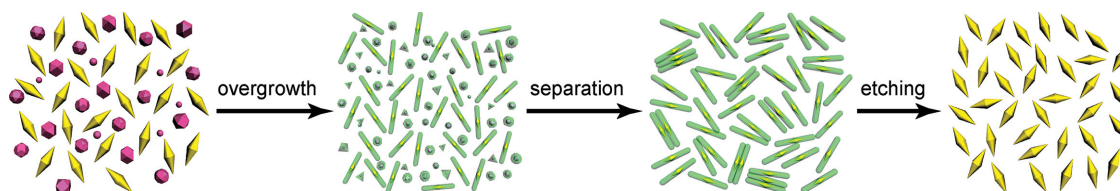


Figure 1. Schematic illustrating the Au NBP purification steps.

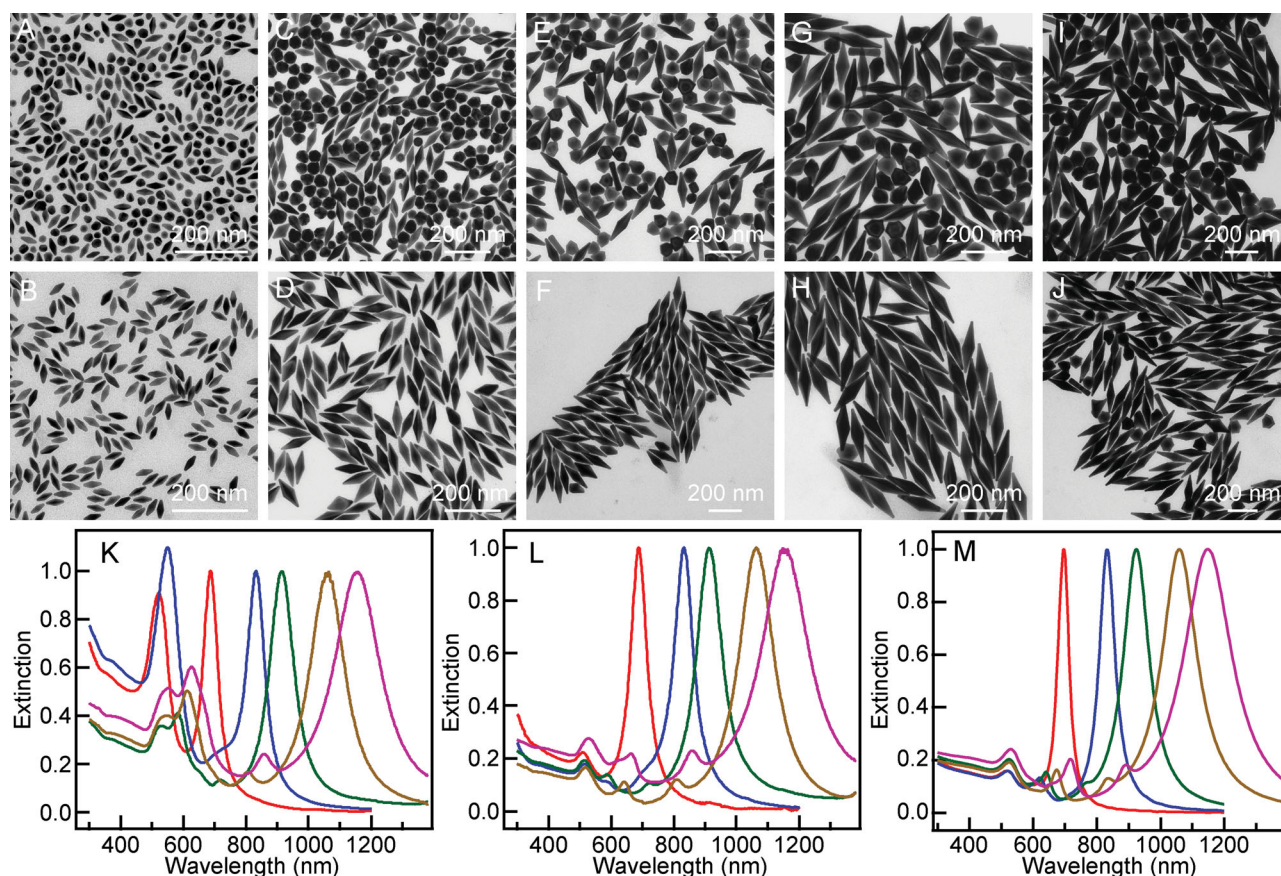


Figure 2. TEM images and extinction spectra of the five Au NBP samples. In the first and second rows are the TEM images of the samples before and after purification, respectively. The LPRWs of the five samples are A,B) 690 nm, C,D) 833 nm, E,F) 914 nm, G,H) 1062 nm, and I,J) 1155 nm, respectively. K,L) Extinction spectra of the five Au NBP samples before and after purification, respectively. M) FDTD-simulated extinction spectra of the five samples. The extinction spectra of the same sample are plotted in the same color in (K–M). All of the extinction spectra have been normalized against the longitudinal plasmon peak maxima.

more than half of the nanoparticles in the products are approximately spherical. In comparison, Au NBPs are dominant in each purified sample, with highly uniform shapes and sizes. The spherical nanoparticle impurities that were existent in the starting Au NBP sample resulted in a relatively strong plasmon peak in the spectral region from 500 to 650 nm (Figure 2K). The intensity of this peak was dramatically reduced after purification (Figure 2L). The striking intensity reduction suggests the removal of the spherical nanoparticle impurities and the dominant presence of Au NBPs. The successful purification was also verified with scanning electron microscopy (SEM) imaging (Figure S1, Supporting Information), which was performed on the three larger Au NBP samples. The SEM images confirm that almost all of the spherical nanoparticles are removed.

We measured the sizes of the Au NBPs from their TEM images both before and after purification and calculated the averages. The number percentages of Au NBPs were obtained by counting the particles on the TEM images. In addition, the FWHM value in wavelength was determined by fitting the experimental extinction spectrum of each ensemble sample with the Lorentzian function. To obtain the FWHM value in energy, the extinction spectrum was converted from wavelength into energy and then subjected to Lorentzian fitting. All of

the obtained results are listed in Table 1. The average lengths, diameters, and aspect ratios are the same within the experimental measurement errors for each sample. They all increase with increasing LPRWs. The FWHM values in wavelength increase as the NBPs become larger, while those in energy vary in the range of 135–180 meV. The number percentages of Au NBPs before purification are in the range from 35% to 60%. After purification, the number percentages of Au NBPs are all improved to be above 92%, with three of them being higher than 95%. The successful purification of all of the five samples strongly suggests that our approach is applicable to Au NBPs with varying aspect ratios.

We conducted finite-difference time-domain (FDTD) simulations to gain a better understanding of the plasmon nature of Au NBPs (see the Supporting Information for the simulation details). The geometrical parameters, including the length, diameter, tip angle, and tip radius, were slightly adjusted around their measured average values so that the calculated LPRWs were as close as possible to the experimental ones for each sample (Figure S2, Supporting Information). Care was also taken to tilt the excitation light propagation direction to be in between the transverse and longitudinal axes (Figure S3, Supporting Information), because the even-parity plasmon modes

Table 1. LPRWs, sizes, number percentages, and longitudinal plasmon peak widths of the five Au NBP samples.

LPRW [nm]	Length [nm] ^{a)}	Diameter [nm] ^{a)}	Aspect ratio ^{a)}	Number percentage [%] ^{a)}	FWHM [nm/meV]	
					Experiment ^{b)}	FDTD ^{b)}
690	49 ± 3	19 ± 1	2.5 ± 0.1	42.7	59.8/153.9	37.8/97.8
	50 ± 2	20 ± 1	2.5 ± 0.1	98.7		
833	117 ± 9	36 ± 3	3.2 ± 0.2	34.9	76.8/136.4	62.7/105.6
	118 ± 11	37 ± 4	3.2 ± 0.1	96.9		
914	191 ± 9	53 ± 4	3.6 ± 0.2	43.5	94.6/142.1	112.5/164.4
	192 ± 8	54 ± 4	3.6 ± 0.1	94.4		
1062	230 ± 6	59 ± 3	3.9 ± 0.2	48.1	131.2/149.6	135.5/154.9
	229 ± 6	59 ± 2	3.9 ± 0.1	96.3		
1155	276 ± 11	70 ± 6	4.0 ± 0.4	59.8	168.7/178.9	172.9/175.2
	278 ± 8	70 ± 4	4.0 ± 0.1	92.2		

^{a)}For the length, diameter, aspect ratio, and number percentage, in the top and bottom rows are the values measured before and after purification, respectively. The length was measured between the opposite tips, and the diameter was measured at the waist for each Au NBP; ^{b)}The experimental values were obtained from the ensemble samples, and the FDTD results were obtained from the single averagely-sized nanoparticles.

of elongated metal nanocrystals can be excited only with such incident plane waves.^[56] The simulated extinction spectra for the five samples after normalization are plotted in Figure 2M. For ease of comparison, they are also drawn together with the experimental ones upon normalization (Figure S4, Supporting Information), or together among themselves without normalization (Figure S5, Supporting Information). The simulated extinction cross-section at the longitudinal plasmon peak increases rapidly with the NBP size. The simulated extinction spectra are in reasonably good agreement with the experimental ones. The number of plasmon peaks increases from 2 to 4 with increasing NBP sizes. The simulated positions for the highest-energy plasmon peak are very close to the experimental ones, but the weak peaks located in the middle spectral range show relatively large discrepancies. The discrepancies are generally believed to be caused by the limitations in modeling the exact geometry of the Au NBPs. Taking the 914-nm sample as an example, we also elucidated the nature of each plasmon mode by simulating the charge distribution contours of the four plasmon peaks (Figure S6, Supporting Information). In the order from high to low energies, the four plasmon modes can be ascribed to be transverse dipolar, longitudinal octupolar, longitudinal quadrupolar, and longitudinal dipolar, respectively.

To further illustrate the purification process, we took the 690-nm Au NBP sample as an example and acquired the TEM images and extinction spectra of both the faceted (Au core)@ (Ag shell) nanoparticles and Au/Ag heteronanorods that were generated in the intermediate steps (Figure 3A). After CTAB was added at a controlled concentration, the depletion-induced attractive potential between the heteronanorods was much larger than that between the faceted nanoparticles. The attractive potential led to the preferential precipitation and purification of the heteronanorods (Figure 3B). Silver was seen to grow uniformly on each Au NBP, as suggested by the narrow length and diameter distributions of the heteronanorods. The surfaces of the heteronanorods are smooth. Their average diameter is only slightly larger than that of the corresponding NBPs. The Au NBPs are dominantly located at the center of the

heteronanorods. Only occasionally were they observed to be located away from the center. Even in this case, the heteronanorods have approximately the same length as the others.

Figure 3C shows the extinction spectra of the starting, intermediate, and end products throughout the purification process. The extinction spectrum of the finally purified product overlaps well with that of the starting sample at the longitudinal

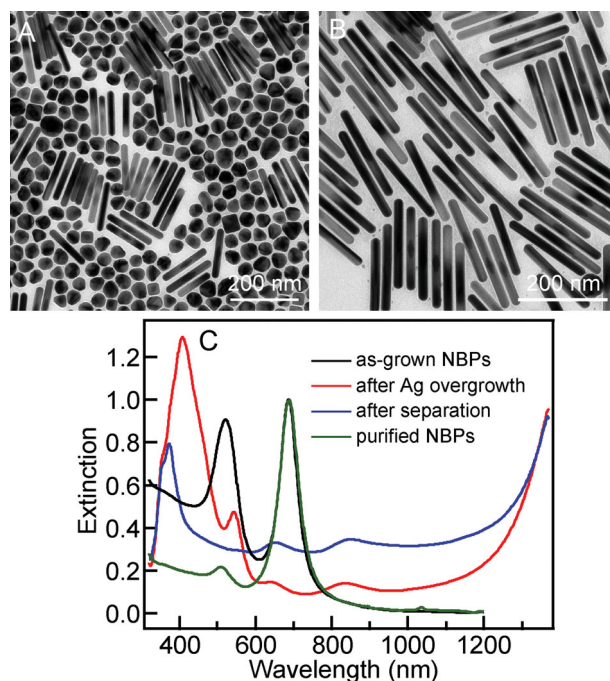


Figure 3. Purification process with the 690-nm Au NBP sample as an example. A,B) TEM images of the Au/Ag heteronanorods before and after separation, respectively. The heteronanorods are 193 ± 18 nm in length and 22 ± 1 nm in diameter. C) Extinction spectra of the as-grown Au NBPs, Au/Ag heteronanorods before and after separation, and purified NBPs.

plasmon peak. This observation suggests clearly that the size and shape of the Au NBPs are maintained after purification. Two additional peaks are seen on the extinction spectrum of the product right after Ag overgrowth in comparison to that after separation. The peak around 410 nm arises from the (Au core)@(Ag shell) nanoparticles, while the peak around 540 nm might come from the nanoparticle impurities with tetrahedral or cubic shapes (Figure 3A). The plasmon peaks around 355 and 370 nm arise from the plasmon resonance of bulk Ag and the transverse plasmon mode of the Au/Ag heteronanorods, respectively.^[57,58] Both of the extinction spectra of the Ag-overgrown products before and after separation possess two plasmon peaks around 650 and 840 nm, which are ascribed to the multipolar longitudinal plasmon resonances.^[59]

In order to verify the complete etching of Ag off Au NBPs, we measured the amounts of Au and Ag in the purified Au NBP samples by inductively coupled plasma atomic emission spectrometry (ICP-AES) and compared the results with those of the as-grown Au NBP samples. Two as-grown and two purified NBP samples were measured. Their LPRWs were in the range from 800 to 850 nm (Figure S7, Supporting Information). The linear relationship between the emission intensity and the atomic mass concentration was pre-calibrated carefully right before each ICP-AES measurement (Figure S8, Supporting Information). The Au molar concentrations for the two as-grown NBP samples were determined to be $(30.9 \pm 0.01) \times 10^{-6}$ and $(147.9 \pm 0.01) \times 10^{-6}$ M. The corresponding Ag molar concentrations were $(3.4 \pm 4.7) \times 10^{-6}$ and $(7.2 \pm 1.0) \times 10^{-6}$ M, respectively. The presence of Ag atoms in the as-grown Au NBP samples is because AgNO₃ is used in seed-mediated growth to increase the number yields of elongated Au nanocrystals.^[7,11,35,36,39] Ag atoms are adsorbed on as-grown Au nanocrystals. The molar ratios between Ag and Au for the two as-grown NBP samples were found to be 0.11 ± 0.15 and 0.05 ± 0.01 , respectively. In comparison, for the two purified Au NBP samples, the Au molar concentrations were $(126.4 \pm 0.01) \times 10^{-6}$ and $(81.7 \pm 0.01) \times 10^{-6}$ M, and the corresponding Ag molar concentrations were $(11.8 \pm 0.3) \times 10^{-6}$ and $(13.9 \pm 0.2) \times 10^{-6}$ M. The molar ratios between Ag and Au were 0.09 ± 0.002 and 0.17 ± 0.002 , respectively. The molar ratios of Ag to Au for the as-grown Au NBP samples were similar to those for the purified samples. Our values are slightly larger than those measured in a previous study for single-crystalline Au NRs,^[60] probably because the molar ratios of Ag to Au in our NBP growth solution are larger than those in that study. Our ICP-AES results therefore confirmed the complete etching of the Ag segments off the heteronanorods to give purified Au NBPs.

We have shown above our method for purifying Au NBPs with number percentages approaching 100%. In order to better evaluate the plasmonic properties of Au NBPs and facilitate their future plasmonic applications, we carried out careful comparison studies between purified Au NBP samples and high-yield Au NR samples in four aspects, which were single-particle dark-field scattering, RIS, TPPL, and SERS. The Au NR samples were prepared using the seed-mediated growth method with the addition of AgNO₃ in the growth solution.^[7,11] They are single-crystalline. The comparison results are described below.

2.2. Single-Particle Dark-Field Scattering

To compare the single-particle scattering properties, one Au NBP sample and one Au NR sample were prepared. The TEM images of the two samples are shown in Figure 4A,B, and their extinction spectra are displayed in Figure 4C. The ensemble LPRWs of the two samples in aqueous solutions were both 682 nm, with the FWHM values being 60 and 105 nm for the Au NBP and NR samples, respectively. Both samples were deposited on glass slides at low surface number densities, which were verified by the dark-field scattering images (Figure 4D,E). The single-particle scattering spectra indicate that the Au NBPs possess narrower peak widths than the Au NRs and that the distribution of the LPRWs of the Au NBPs is smaller than that of the Au NRs (Figure 4F,G).

We collected the scattering spectra of more than 60 individual nanoparticles for each sample and plotted the histograms of the LPRWs and FWHM values (Figure 4H–K). The obtained average LPRWs and FWHM values, together with the average lengths and diameters determined from the TEM images, are summarized in Table 2. The average FWHM value obtained from the single-particle scattering measurements for the Au NBPs is 48 ± 3 nm, which is very close to the ensemble FWHM value of 60 nm. This closeness suggests that the purified Au NBP sample is highly uniform in shape and size. In contrast, for the Au NR sample, the average FWHM value from the single-particle scattering measurements is 59 ± 4 nm, which is about a half of the corresponding ensemble value of 105 nm. This result suggests that the Au NR sample has larger distributions in shape and size. The LPRWs of the Au NBP and NR samples are very close to each other, but the average single-particle FWHM value of the Au NBP sample is smaller than that of the NR sample. The smaller plasmon peak width implies that the Au NBPs have a smaller plasmon damping and a larger electric field enhancement than the Au NRs.^[61] In addition, for both samples, the average LPRWs determined from the single-particle scattering measurements are smaller than the ensemble solution values. This is because the average refractive index of the surrounding environment of the Au nanocrystals deposited on glass slides is smaller than that in water.

2.3. Refractive Index Sensing

The ensemble LPRWs of the Au NBP and NR samples used for the RIS and FOM comparison are 842 and 856 nm, respectively. The Au nanocrystals were either dispersed in water–glycerol mixtures of different compositions by centrifugation, or deposited on mesoporous TiO₂ substrates, followed by immersion into different water–glycerol mixtures. The consideration of the substrate case is because many sensing applications require the deposition of metal nanocrystals on substrates to avoid the aggregation of metal nanocrystals when they are exposed to different liquid environments. Figure 5A,B show the TEM images of the two samples. The extinction spectra are displayed in Figure 5C. The deposited Au NBPs and NRs are relatively densely and uniformly distributed on the substrates, with the surface number densities being ≈ 160 and $\approx 150 \mu\text{m}^{-2}$,

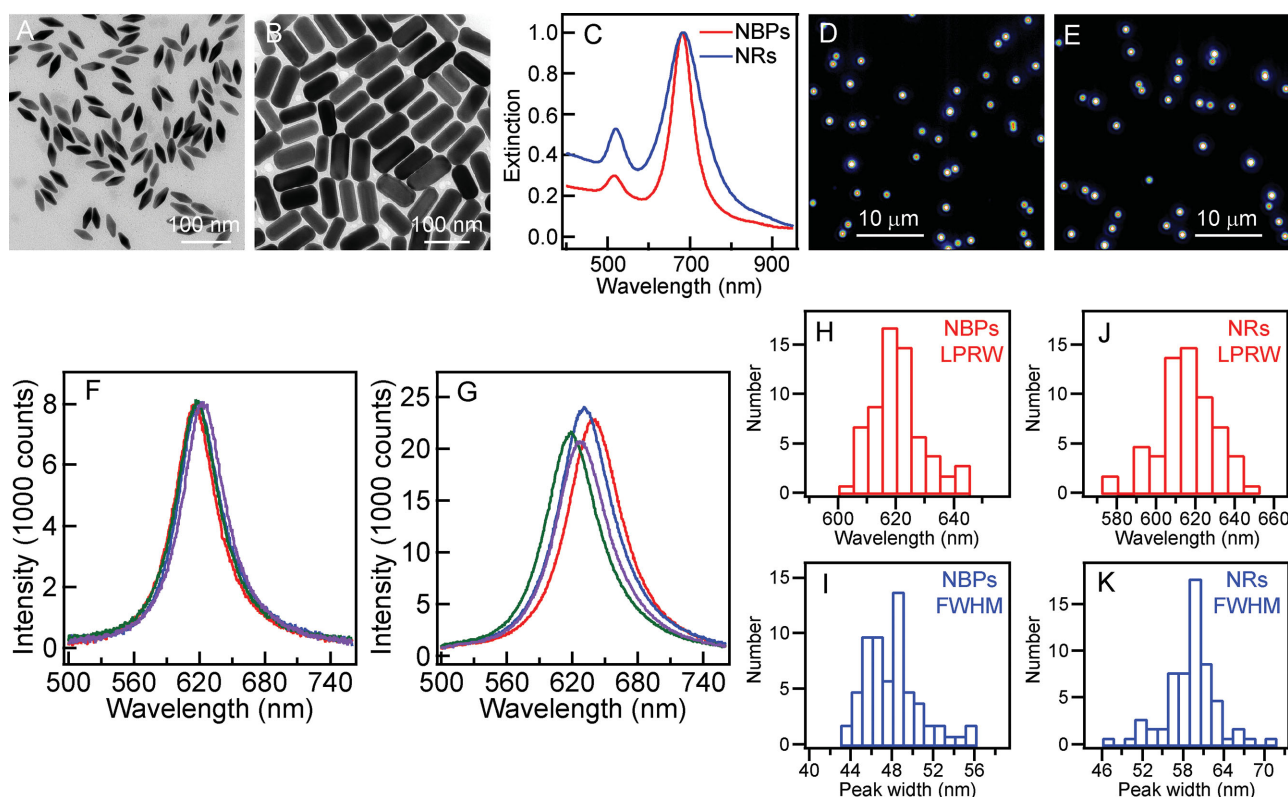


Figure 4. Comparison of the single-particle dark-field scattering results between Au NBP and NR samples. A,B) TEM images of the Au NBP and NR samples, respectively. C) Normalized extinction spectra of the two samples dispersed in aqueous solutions. D,E) Dark-field scattering images of the Au NBP and NR samples, respectively. F,G) Five representative single-particle scattering spectra for the Au NBP and NR samples, respectively. H–K) Histograms of the LPRWs and FWHM values for the Au NBP and NR samples.

respectively (Figure 5D,E). Water–glycerol mixtures with the volume percentage of glycerol varied among 0%, 10%, 30%, 50%, 70%, and 90% were used to change the refractive index of the surrounding medium of the Au nanocrystals. The refractive indices of water and glycerol are 1.3334 and 1.4746, respectively. The refractive indices of the liquid mixtures were calculated according to the Lorentz–Lorenz equation.^[31,40] Figure S9A,B (Supporting Information) shows the extinction spectra of the Au NBP and NR samples dispersed in the water–glycerol mixtures. The longitudinal plasmon resonance peaks were seen to red-shift as the refractive index of the surrounding environment was increased. Figure 5F shows the variations of the LPRWs as functions of the refractive index. The RISs of the Au NBP and NR samples dispersed in the liquid mixtures were determined to be 362 nm/RIU (refractive index unit) and 303 nm/RIU, indicating that the RIS of the Au NBP sample is higher than that of the Au NR sample. Because the FWHM of the Au NBP sample is smaller, the FOM of the Au NBP sample is more than twice that of the Au NR sample (Table 2). This makes Au NBPs a superior candidate for various sensing applications. When the deposited Au NBP and NR samples were exposed to the liquid mixtures, the longitudinal plasmon peaks were also seen to red-shift with increasing refractive indices (Figure S9C,D, Supporting Information). The resultant RISs and FOM values are listed in Table 2. Again, both the RIS and FOM of the deposited Au NBP sample are higher than the corresponding values of the deposited Au NR sample.

2.4. Two-Photon Photoluminescence

Two-photon excitation provides unprecedented capabilities of activating chemical and/or physical processes with high spatial resolution in three dimensions and has made possible the development of three-dimensional fluorescence imaging,^[62] optical data storage,^[63] and microfabrication.^[64] Au NRs have been known to exhibit about two orders of magnitude larger two-photon extinction cross-sections than organic dye molecules.^[65–69] In this regard, we measured the TPPL properties of Au NBPs and compared them with those of Au NRs with equal LPRWs. Two pairs of Au NBP and NR samples were prepared for this purpose (Figure 6A–D). One pair had the LPRW at 744 nm, and the other at 840 nm (Figure 6E). In order to make better comparison, we considered the particle concentrations of the samples. Experimentally, the particle concentration can be estimated from the Au mass concentration measured with ICP-AES (Figure S10, Supporting Information) and the average nanocrystal sizes determined from the TEM images. For the TPPL measurements, the particle concentrations of the two samples in each pair were adjusted to be the same, with those of the 744- and 840-nm pairs being 1.6×10^{11} and 7.0×10^{11} mL⁻¹, respectively. Figure 6F presents the TPPL spectra of the four samples. To verify the two-photon excitation nature of the emission, the excitation power dependencies were examined. The acquired log–log plots of the integrated TPPL intensity

Table 2. Comparison of the plasmonic properties between Au NBPs and Au NRs.

Property	Parameter	NR	NBP	NBP-to-NR ratio
Single-particle dark-field scattering	Length [nm]	92 ± 8	51 ± 2	
	Diameter [nm]	39 ± 6	20 ± 1	
	LPRW [nm] ^{a)}	615 ± 15	620 ± 9	
	FWHM [nm] ^{a)}	59 ± 4	48 ± 3	0.81 ± 0.06
Refractive index sensing ^{b)}	LPRW [nm]	856/865	842/865	
	Length [nm]	79 ± 9	105 ± 5	
	Diameter [nm]	18 ± 2	31 ± 1	
	RIS [nm/RIU]	303/324	362/384	1.2/1.2
	FWHM [nm]	151/180	86/107	0.57/0.59
	FOM	2.0/1.8	4.2/3.6	2.1/2.0
TPPL	744 nm ^{c)}	Length [nm]	70 ± 8	93 ± 4
		Diameter [nm]	21 ± 2	32 ± 2
		σ_{ext} [10 ⁻¹⁵ m ² , experiment/ FDTD] ^{d)}	4.0 ± 1.0/12.6	8.7 ± 1.1/13.8
		Intensity ^{e)}	499 000	2 040 000
	840 nm ^{c)}	Length [nm]	62 ± 9	99 ± 4
		Diameter [nm]	14 ± 2	29 ± 2
		σ_{ext} [10 ⁻¹⁵ m ² , experiment/ FDTD] ^{d)}	2.5 ± 0.8/7.7	7.0 ± 1.0/13.7
		Intensity ^{f)}	482 000	6 527 000
SERS ^{g)}	Length [nm]	68 ± 10/78 ± 7	83 ± 3/106 ± 5	
	Diameter [nm]	17 ± 3/19 ± 2	25 ± 1/30 ± 2	
	LPRW [nm]	793/784	793/780	
	Intensity [counts] ^{h)}	180/470	1080/8560	6.0/18.2

^{a)}Determined from the single-particle dark-field scattering spectra; ^{b)}The RISs were measured in solutions and on substrates. The values before and after the slash symbol were measured in solutions and on substrates, respectively; ^{c)}The particle concentrations for the 744- and 840-nm samples were 1.6×10^{11} and 7.0×10^{11} mL⁻¹, respectively; ^{d)} σ_{ext} denotes the extinction cross-section. Both the experimental and FDTD-calculated values were determined; ^{e)}TPPL intensity integrated from 375 to 650 nm. The excitation laser power was 50 mW; ^{f)}TPPL intensity integrated from 375 to 710 nm. The excitation laser power was 50 mW; ^{g)}The values for SERS before and after the slash symbol were measured in aqueous solutions and on substrates, respectively; ^{h)}The Raman peak intensity around 1080 cm⁻¹.

as a function of the excitation laser power showed a linear relationship with slopes of ≈ 2.0 for all of the four samples (Figure S11, Supporting Information), suggesting a two-photon excitation process. We integrated the TPPL intensities from 375 to 650 nm for the 744-nm samples and from 375 to 710 nm for the 840-nm samples at an excitation laser power of 50 mW. The results are listed in Table 2. The Au NBP samples were found to perform better in TPPL than the NR samples. The TPPL intensity of the 744-nm Au NBP sample was 4.1 times that of the 744-nm Au NR sample, and the TPPL intensity ratio between the 840-nm Au NBP and NR samples was 13.5. The higher TPPL intensity possessed by Au NBPs will be useful for two-photon biological imaging and photo-thermal therapy.

As mentioned above, the particle concentrations of the Au NBP and NR samples were obtained by ICP-AES. On the basis of the particle concentrations, we can estimate the extinction cross-sections of the nanocrystals samples. The extinction cross-section σ_{ext} of a single nanocrystal can be determined according to

$$E = \frac{N\sigma_{\text{ext}}l}{2.303} \quad (2)$$

where E is the extinction value at the LPRW, N is the particle concentration, and l is the optical path length. The extinction value was obtained by measuring the extinction spectrum of each sample (Figure 6E). The determined extinction cross-sections of the four Au NBP and NR samples used in the TPPL measurements are given in Table 2. The Au NBPs possess higher extinction cross-sections than the Au NRs with the same LPRWs, because of the larger particle volumes of the former. On the other hand, the extinction cross-sections calculated by FDTD simulations were found to be larger than the experimental ones for all of the four samples. The discrepancies can be attributed mainly to the presence of nanoparticle impurities and inhomogeneous size distributions in the Au nanocrystal samples. The nanoparticle impurities caused over-estimation of the particle concentrations of the NBPs and NRs during the ICP-AES measurements, which in turn resulted in under-estimation of the experimental extinction cross-sections according

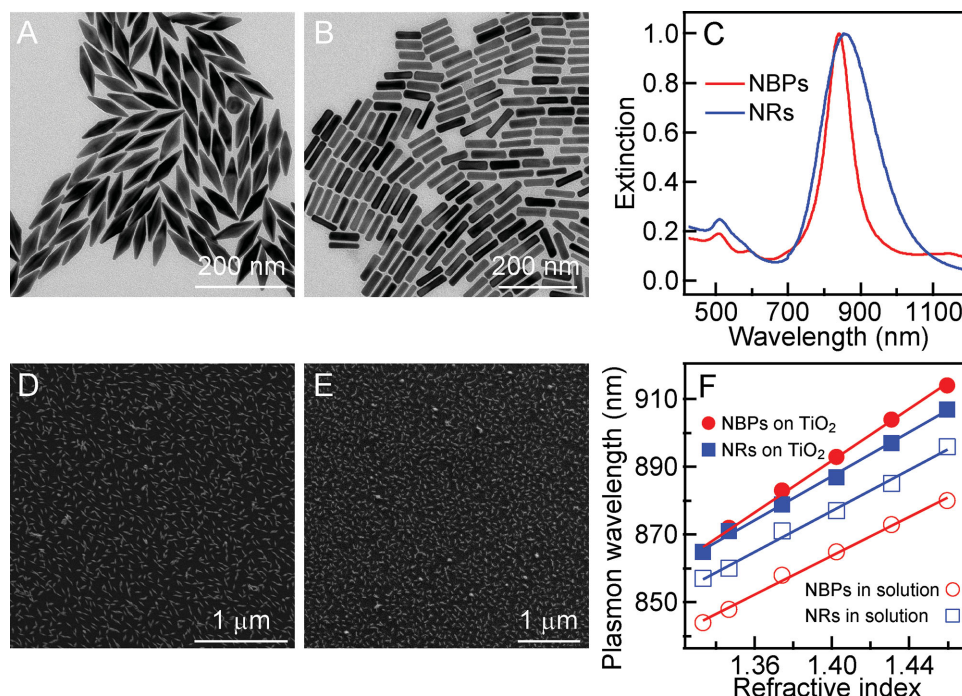


Figure 5. Comparison of the RISs and FOM values between Au NBPs and NRs. A,B) TEM images of the Au NBP and NR samples, respectively. C) Normalized extinction spectra of the NBP and NR samples dispersed in aqueous solutions. D,E) SEM images of the Au NBP and NR samples deposited on mesoporous TiO_2 substrates. F) Dependences of the LPRW on the refractive index of the liquid mixture for the Au NBP and NR samples in solutions and on substrates. The lines are linear fits. The coefficients of determination for the fitting are $R^2 = 0.9942, 0.9976, 0.9921$, and 0.9973 for the NBPs in solutions, the NBPs on substrates, the NRs in solutions and the NRs on substrates, respectively.

to Equation (2). In the case of the size and shape inhomogeneities, the NBPs and NRs with LPRWs slightly different from the ensemble peak wavelengths contributed less to the total extinction value at the ensemble peak wavelengths. Therefore,

the experimentally determined extinction cross-sections were smaller. The reasoning above is also consistent with the fact that the discrepancies between the experimental and simulation values are smaller for the Au NBP samples than those for

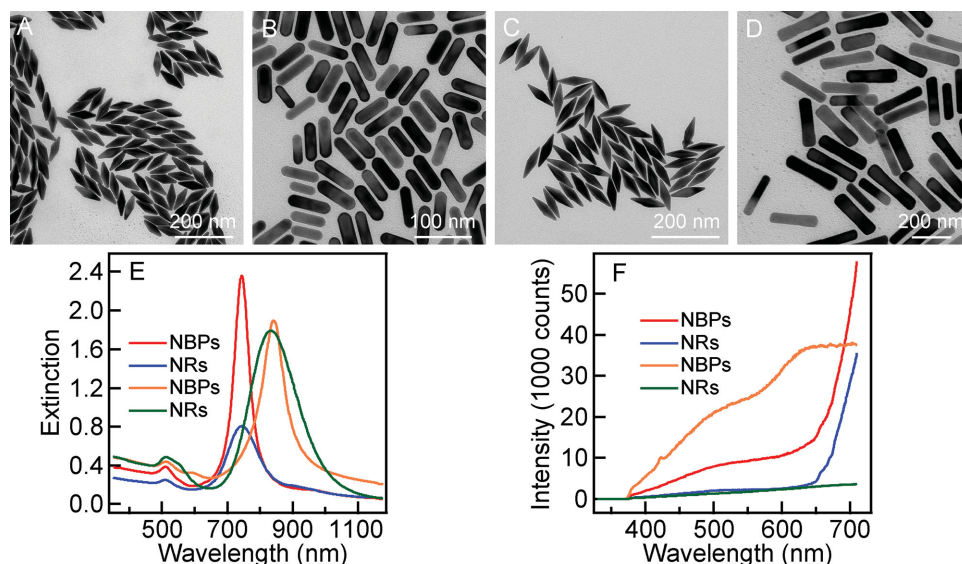


Figure 6. Comparison of the TPPL properties between Au NBPs and NRs. A,B) TEM images of the 744-nm Au NBP and NR samples, respectively. C,D) TEM images of the 840-nm Au NBP and NR samples, respectively. E) Extinction spectra of the samples dispersed in aqueous solutions. F) TPPL spectra of the four samples. The labels for the spectra correspond to those in E) for the different Au nanocrystal samples. The excitation laser wavelengths for the 744- and 840-nm samples were 750 and 840 nm, respectively. The rising intensities toward the long-wavelength region for the 744-nm samples is due to the incomplete blocking of the excitation laser light by use of a 750-nm short-pass filter.

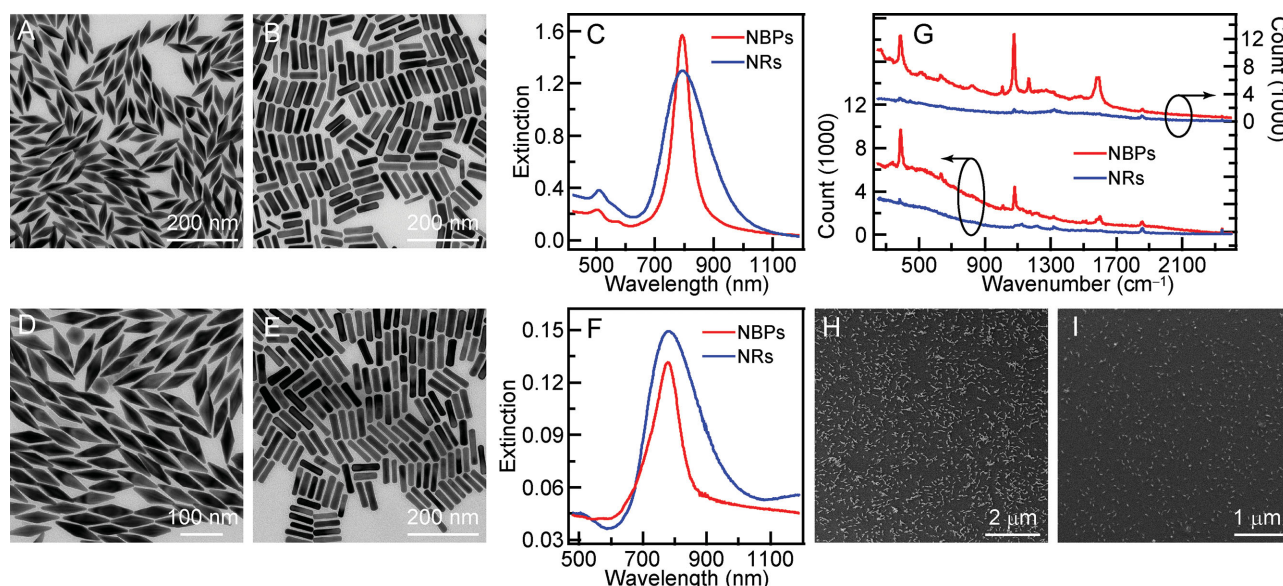


Figure 7. Comparison of the SERS performances between Au NBPs and NRs. A,B) TEM images of the Au NBP and NR samples used for the measurements in solutions, respectively. C) Extinction spectra of the Au NBP and NR samples used for the solution measurements. D,E) TEM images of the Au NBP and NR samples used for the measurements on substrates, respectively. F) Extinction spectra of the Au NBP and NR samples used for the substrate SERS measurements. G) Raman signals of 4-mercaptophenol adsorbed on the Au NBP and NR samples. The top two spectra are for the samples deposited on substrates, and the bottom two are for the samples dispersed in solutions. H,I) SEM images of the Au NBP and NR samples deposited on mesoporous TiO_2 substrates, respectively.

the NR samples, because the Au NBP samples have less impurities and are more homogeneous than the Au NR samples.

2.5. Surface-Enhanced Raman Scattering

The narrower peak widths and larger electric field enhancements of Au NBPs are beneficial to plasmon-enhanced spectroscopy. We further compared the SERS performances between Au NBPs and NRs that were dispersed in solutions or deposited on substrates. Previous studies have shown that adjustment of the plasmon wavelength in between the excitation laser and Raman emission wavelength gives maximal Raman intensity enhancements.^[70] In our SERS studies, two pairs of Au NBP and NR samples were prepared for the measurements in solutions and on substrates, respectively (Figure 7A–F). Because the excitation laser wavelength was 785 nm, the LPRWs of the samples were synthetically adjusted to be slightly longer than 785 nm, as listed in Table 2. 4-mercaptophenol was chosen as a Raman-active probe. For the SERS measurements in aqueous solutions, the particle concentrations of the Au NBP and NR samples were determined according to the measured peak extinction values and the estimated extinction cross-sections (Equation (2)). They were then adjusted to be the same at $\approx 1.2 \times 10^{11} \text{ mL}^{-1}$. The concentration of the stock solution of 4-mercaptophenol was $1 \times 10^{-3} \text{ M}$, with NaOH added at $12 \times 10^{-3} \text{ M}$ to enhance the dissolution of the molecule. 10 and 20 μL of the stock probe solution were added into 1 mL of the Au nanocrystal solution, respectively. The resultant probe concentrations in the Au nanocrystal solutions were calculated to be 9.9×10^{-6} and $19.6 \times 10^{-6} \text{ M}$, respectively. These concentrations were higher than the saturation concentrations, which

were the amounts of the probe molecule required for complete adsorption on the total surface areas of all Au nanocrystals at one monolayer. The saturation concentrations were estimated to be 2.97×10^{-6} and $2.78 \times 10^{-6} \text{ M}$ for the Au NBP and NR samples, respectively, using the value of 0.22 nm^2 occupied by one thiol molecule on the Au surface. The bottom two Raman spectra in Figure 7G were obtained for the addition of 20 μL of the stock probe solution, while those for the addition of 10 μL of the stock solution are provided in Figure S12, Supporting Information. The results indicate that the Au NBP sample gives much stronger SERS signals than the Au NR sample. On the other hand, the SERS signals for the addition of 20 and 10 μL of the stock probe solution are almost the same in intensity, verifying that the added amounts of the probe molecule were in excess for adsorption. We obtained the peak intensity at 1080 cm^{-1} (Table 2) and found that the intensity with the Au NBP sample is ≈ 6 times that of the Au NR sample. In addition, we also carried out SERS measurements with the nanocrystal samples deposited on mesoporous TiO_2 substrates (Figure 7H,I). The surface number densities of the deposited Au NBPs and NRs are 22.5 and $33.2 \mu\text{m}^{-2}$, respectively. The substrates with the deposited nanocrystals were immersed in the 4-mercaptophenol solution for adsorption. The peak intensity at 1080 cm^{-1} for the Au NBP sample was found to be 18.2 times that for the Au NR sample (Table 2). During the SERS comparisons in solutions and on substrates, we simply considered the peak intensities, without taking into account the numbers and total surface areas of the Au nanocrystals. The SERS enhancements are contributed dominantly by the tip regions of the individual, unassembled Au NBPs and NRs.^[71] The exact number of the molecules adsorbed to the tip region is unknown at this stage.

3. Conclusions

A method for producing Au NBPs with number percentages approaching 100% has been demonstrated. The method is based on seed-mediated growth, Ag overgrowth, depletion-induced self-separation, and chemical etching. The obtained Au NBPs are highly uniform in size and shape. Their LPRWs can be synthetically tuned broadly from the visible to near-infrared region. The sharp tips brought about by the inherent crystalline structure enable Au NBPs with large electric field enhancements. We have carefully compared the plasmonic properties between Au NBPs and single-crystalline Au NRs and found that in comparison with Au NRs, Au NBPs possess narrower peak widths, higher RISs, and FOM values, stronger TPPL and larger SERS enhancements. Taken together, our results show unambiguously that Au NBPs will be an attractive candidate for various plasmonic applications in sensing, biomedicine, and plasmon-enhanced spectroscopies.

4. Experimental Section

Chemicals: Gold chloride trihydrate ($\text{HAuCl}_4 \cdot 3\text{H}_2\text{O}$, 99%), sodium borohydride (NaBH_4 , 98%), silver nitrate (AgNO_3 , 99%), ascorbic acid (99%), CTAC in water (25 wt%), trisodium citrate (99%), and 4-mercaptophenol (97%) were purchased from Sigma-Aldrich. CTAB (98%) was obtained from Alfa Aesar. Ammonia solution (25 wt%) was ordered from E. Merck (Germany). Hydrogen peroxide solution (30 wt%) was purchased from Aladdin Chemical (China). CTBAB was synthesized by refluxing stoichiometric amounts of 1-bromohexadecane (97%, Aldrich) and tributylamine (98.5%, Aldrich) in dry acetonitrile for 48 h, as described previously in our work.^[39]

Au NBP Growth: The Au NBP samples were prepared using the seed-mediated growth method, as described in the previous works.^[35,36,39] Specifically, the citrate-stabilized seed solution was made by adding a freshly prepared, ice-cold NaBH_4 solution (0.01 M, 0.15 mL) into an aqueous solution composed of HAuCl_4 (0.01 M, 0.125 mL), trisodium citrate (0.01 M, 0.25 mL), and water (9.625 mL) under vigorous stirring. The resultant seed solution was kept at room temperature for 2 h before use. The CTAB growth solution was prepared by sequential addition of HAuCl_4 (0.01 M, 2 mL), AgNO_3 (0.01 M, 0.4 mL), HCl (1 M, 0.8 mL), and ascorbic acid (0.1 M, 0.32 mL) into an aqueous CTAB solution (0.1 M, 40 mL). The seed solution (0.1–2 mL) was then added into the growth solution, followed by gentle inversion mixing for 10 s. The reaction solution was left undisturbed overnight at room temperature. The LPRWs of the Au NBP samples grown in the CTAB growth solutions could be varied from 680 to 850 nm. The 690- and 833-nm Au NBP samples used in this work were obtained by use of 2 and 0.2 mL of the seed solution, respectively. The CTBAB growth solution was prepared by sequential addition of HAuCl_4 (0.01 M, 0.3 mL), ascorbic acid (0.1 M, 0.1 mL), and AgNO_3 (0.01 M, 0.15 mL) into an aqueous CTBAB solution (0.01 M, 7.125 mL). The citrate-stabilized seed solution (0.05–0.4 mL) was then added. The reaction solution was mixed by gentle inversion for 10 s and left undisturbed overnight in an oven at 65 °C. The CTBAB growth solutions were employed to grow Au NBPs with longer LPRWs. The added amounts of the seed solution were 100, 80, and 50 mL for the growth of the 914-, 1062-, and 1155-nm Au NBP samples, respectively.

Au NR Growth: All of the Au NR samples were prepared by seed-mediated growth, as described in the previous works by us and others.^[7,11,20–22,36,40] The LPRWs of the Au NR samples were synthetically adjusted to the desired values by varying the seed amount relative to the growth solution volume together with anisotropic shortening.

Au NBP Purification: The as-grown Au NBP sample (40 mL) of a certain size was centrifuged at 6000–8000 rpm for 10 min. The precipitate was

redispersed in a CTAC solution (0.08 M, 30 mL), which was followed by subsequent addition and mixing of AgNO_3 (0.01 M, 6 mL) and ascorbic acid (0.1 M, 3 mL). The resultant solution was kept in an oven at 65 °C for 4 h, during which Ag was overgrown on the Au nanocrystals to produce bimetallic Au/Ag products. The volume of the AgNO_3 solution added into the Au NBP solution could be varied from 6 to 10 mL. The bimetallic Au/Ag products were then centrifuged at 5000 rpm for 10 min. The precipitate was redispersed in CTAB (0.05 M, 30 mL) and left undisturbed for ≈ 4 h at room temperature, during which the Au/Ag heteronanorods agglomerated together and precipitated to the bottom of the container, while the spherical (Au core)@(Ag shell) nanoparticles remained in the supernatant. The supernatant was discarded. The remaining Au/Ag heteronanorods were redispersed in water (20 mL). The resultant solution was subsequently mixed gently with $\text{NH}_3 \cdot \text{H}_2\text{O}$ (30 wt%, 0.4 mL) and H_2O_2 (0.1 M, 0.3 mL) and kept undisturbed for 4 h. During this process, the Ag segments were gradually etched away. AgCl precipitate was seen to form at the bottom of the container. The clear supernatant was carefully taken out and centrifuged at ≈ 5000 rpm for 10 min. The product was redispersed in a CTAB solution (0.05 M, 10 mL) or water for further use.

Characterization: Extinction spectra were recorded on a Hitachi U-3501 UV/visible/near infrared spectrophotometer with standard 0.5-cm cuvettes. SEM images were taken on an FEI Quanta 400 FEG microscope at 10 kV. TEM images were taken on an FEI Tecnai Spirit 12 microscope, which was operated at 120 kV. The sizes and number percentages of the Au nanocrystals were measured from their TEM images, with ≈ 100 particles measured for size and ≈ 200 particles counted for number percentage per sample. The Au mass concentrations in the solution samples were measured using an ICP-AES system (PerkinElmer, Optima 4300DV). The mesoporous TiO_2 films were prepared through evaporation-induced self-assembly by dip coating on clean glass slides, following our reported procedure.^[72,73] The Au nanocrystals were deposited by immersing the TiO_2 substrates in the nanocrystal solutions at controlled CTAB concentrations for ≈ 2 h, following our recently described method.^[73]

Single-particle dark-field scattering spectra were recorded on an upright optical microscope (Olympus, BX60) that was integrated with a quartz-tungsten-halogen lamp (100 W), a monochromator (Acton, SpectraPro 2300i), and a charge-coupled device camera (Princeton Instruments, Pixis 512B). During the measurements, the camera was thermoelectrically cooled to -70 °C. A dark-field objective (50 \times , numerical aperture 0.5) was employed for both exciting the individual nanoparticles with white light and collecting the scattered light. The scattering spectrum from an individual nanoparticle was corrected by first subtracting the background spectrum taken from the adjacent region without any nanoparticles and then dividing it with a pre-calibrated response curve of the entire optical system. The exposure time was set at 30 s.

The TPPL measurements were performed using a femtosecond Ti:sapphire oscillator (Avesta, TiF-100M) as the excitation source. The output laser pulses had a tunable center wavelength from 740 to 860 nm with pulse duration of 80 fs and a repetition rate of 84.5 MHz. The laser beam was focused on the sample that was contained in a quartz cuvette with a path length of 1 cm. The emission from the sample was collected at an angle of 90° with a pair of lenses and an optical fiber that was connected to a monochromator (Acton, SpectraPro 2300i) coupled with a charge-coupled device camera (Princeton Instruments, Pixis 100B). A 750-nm short-pass filter was placed in front of the spectrometer to minimize the scattering from the pump beam.

The Raman spectra were collected from the Au nanocrystal samples either dispersed in aqueous solutions or deposited on the TiO_2 substrates on a micro-Raman system (Renishaw, RM 3000), with a diode laser (785 nm, 20 mW) as the excitation source and a 50 \times objective. The exposure time was set at 10 s. After the addition of the 4-mercaptophenol stock solution, the Au nanocrystal solutions were kept at room temperature for more than 4 h to ensure that the adsorption of the molecules on the nanocrystal surfaces reached equilibrium.

Supporting Information

Supporting Information is available from the Wiley Online Library or from the author.

Acknowledgements

This work was supported by Hong Kong RGC through a CRF grant (Grant No. CUHK1/CRF/12G) and a SRFDP/RGC ERG grant (Grant No. M-CUHK410/12).

Received: October 30, 2014

Revised: December 14, 2014

Published online: February 9, 2015

- [1] L. Dykman, N. Khlebtsov, *Chem. Soc. Rev.* **2012**, 41, 2256.
- [2] R. Wilson, *Chem. Soc. Rev.* **2008**, 37, 2028.
- [3] S. Lal, S. E. Clare, N. J. Halas, *Acc. Chem. Res.* **2008**, 41, 1842.
- [4] S. Lal, N. K. Grady, J. Kundu, C. S. Levin, J. B. Lassiter, N. J. Halas, *Chem. Soc. Rev.* **2008**, 37, 898.
- [5] V. Giannini, A. I. Fernández-Domínguez, S. C. Heck, S. A. Maier, *Chem. Rev.* **2011**, 111, 3888.
- [6] S. Linic, P. Christopher, D. B. Ingram, *Nat. Mater.* **2011**, 10, 911.
- [7] W. H. Ni, X. S. Kou, Z. Yang, J. F. Wang, *ACS Nano* **2008**, 2, 677.
- [8] H. J. Chen, L. Shao, Q. Li, J. F. Wang, *Chem. Soc. Rev.* **2013**, 42, 2679.
- [9] L. Vigdeman, B. P. Khanal, E. R. Zubarev, *Adv. Mater.* **2012**, 24, 4811.
- [10] L. Vigdeman, E. R. Zubarev, *Chem. Mater.* **2013**, 25, 1450.
- [11] T. K. Sau, C. J. Murphy, *Langmuir* **2004**, 20, 6414.
- [12] X. C. Ye, C. Zheng, J. Chen, Y. Z. Gao, C. B. Murray, *Nano Lett.* **2013**, 13, 765.
- [13] X. H. Huang, S. Neretina, M. A. El-Sayed, *Adv. Mater.* **2009**, 21, 4880.
- [14] A. S. Stender, K. Marchuk, C. Liu, S. Sander, M. W. Meyer, E. A. Smith, B. Neupane, G. F. Wang, J. J. Li, J.-X. Cheng, B. Huang, N. Fang, *Chem. Rev.* **2013**, 113, 2469.
- [15] Z. Y. Xiao, C. W. Ji, J. J. Shi, E. M. Pridgen, J. Frieder, J. Wu, O. C. Farokhzad, *Angew. Chem., Int. Ed.* **2012**, 51, 11853.
- [16] S. E. Lee, G. L. Liu, F. Kim, L. P. Lee, *Nano Lett.* **2009**, 9, 562.
- [17] W. I. Choi, J.-Y. Kim, C. Kang, C. C. Byeon, Y. H. Kim, G. Tae, *ACS Nano* **2011**, 5, 1995.
- [18] X. H. Huang, I. H. El-Sayed, W. Qian, M. A. El-Sayed, *J. Am. Chem. Soc.* **2006**, 128, 2115.
- [19] G. F. Wang, W. Sun, Y. Luo, N. Fang, *J. Am. Chem. Soc.* **2010**, 132, 16417.
- [20] T. Ming, L. Zhao, Z. Yang, H. J. Chen, L. D. Sun, J. F. Wang, C. H. Yan, *Nano Lett.* **2009**, 9, 3896.
- [21] T. Ming, L. Zhao, H. J. Chen, K. C. Woo, J. F. Wang, H.-Q. Lin, *Nano Lett.* **2011**, 11, 2296.
- [22] L. Zhao, T. Ming, H. J. Chen, Y. Liang, J. F. Wang, *Nanoscale* **2011**, 3, 3849.
- [23] T. Ming, H. J. Chen, R. B. Jiang, Q. Li, J. F. Wang, *J. Phys. Chem. Lett.* **2012**, 3, 191.
- [24] R. A. Alvarez-Puebla, A. Agarwal, P. Manna, B. P. Khanal, P. Aldeanueva-Potell, E. Carbó-Argibay, N. Pazos-Pérez, L. Vigdeman, E. R. Zubarev, N. A. Kotov, L. M. Liz-Marzán, *Proc. Natl. Acad. Sci. U. S. A.* **2011**, 108, 8157.
- [25] L. Vigdeman, E. R. Zubarev, *Langmuir* **2012**, 28, 9034.
- [26] S. Chang, Q. Li, X. D. Xiao, K. Y. Wong, T. Chen, *Energy Environ. Sci.* **2012**, 5, 9444.
- [27] F. Wang, C. H. Li, H. J. Chen, R. B. Jiang, L.-D. Sun, Q. Li, J. F. Wang, J. C. Yu, C.-H. Yan, *J. Am. Chem. Soc.* **2013**, 135, 5588.
- [28] P. Zijlstra, J. W. M. Chon, M. Gu, *Nature* **2009**, 459, 410.
- [29] M. W. Knight, H. Sobhani, P. Nordlander, N. J. Halas, *Science* **2011**, 332, 702.
- [30] G. A. Wurtz, R. Pollard, W. Hendren, G. P. Wiederrecht, D. J. Gosztola, V. A. Podolskiy, A. V. Zayats, *Nat. Nanotechnol.* **2011**, 6, 107.
- [31] H. J. Chen, L. Shao, K. C. Woo, T. Ming, H.-Q. Lin, J. F. Wang, *J. Phys. Chem. C* **2009**, 113, 17691.
- [32] M. Z. Liu, P. Guyot-Sionnest, *Phys. Rev. B* **2007**, 76, 235428.
- [33] M. Z. Liu, T.-W. Lee, S. K. Gray, P. Guyot-Sionnest, M. Pelton, *Phys. Rev. Lett.* **2009**, 102, 107401.
- [34] E. W. Malachosky, P. Guyot-Sionnest, *J. Phys. Chem. C* **2014**, 118, 6405.
- [35] M. Z. Liu, P. Guyot-Sionnest, *J. Phys. Chem. B* **2005**, 109, 22192.
- [36] X. S. Kou, S. Z. Zhang, C.-K. Tsung, M. H. Yeung, Q. H. Shi, G. D. Stucky, L. D. Sun, J. F. Wang, C. H. Yan, *J. Phys. Chem. B* **2006**, 110, 16377.
- [37] M. Pelton, J. E. Sader, J. Burgin, M. Z. Liu, P. Guyot-Sionnest, D. Gosztola, *Nat. Nanotechnol.* **2009**, 4, 492.
- [38] M. Pelton, D. Chakraborty, E. Malachosky, P. Guyot-Sionnest, J. E. Sader, *Phys. Rev. Lett.* **2013**, 111, 244502.
- [39] X. S. Kou, W. H. Ni, C.-K. Tsung, K. Chan, H.-Q. Lin, G. D. Stucky, J. F. Wang, *Small* **2007**, 3, 2103.
- [40] H. J. Chen, X. S. Kou, Z. Yang, W. H. Ni, J. F. Wang, *Langmuir* **2008**, 24, 5233.
- [41] S. Lee, K. M. Mayer, J. H. Hafner, *Anal. Chem.* **2009**, 81, 4450.
- [42] G. J. Zhou, Y. Yang, S. H. Han, W. Chen, Y. Z. Fu, C. Zou, L. J. Zhang, S. M. Huang, *ACS Appl. Mater. Interfaces* **2013**, 5, 13340.
- [43] T. T. Tran, X. M. Lu, *J. Phys. Chem. C* **2011**, 115, 3638.
- [44] B. Schmidt, K. Loeschner, N. Hadrup, A. Mortensen, J. J. Sloth, C. B. Koch, E. H. Larsen, *Anal. Chem.* **2011**, 83, 2461.
- [45] M. Hanauer, S. Pierrat, I. Zins, A. Lotz, C. Sönnichsen, *Nano Lett.* **2007**, 7, 2881.
- [46] W. J. Liu, D. Liu, Z. N. Zhu, B. Han, Y. Gao, Z. Y. Tang, *Nanoscale* **2014**, 6, 4498.
- [47] B. Kowalczyk, I. Lagzi, B. A. Grzybowski, *Curr. Opin. Colloid Interface Sci.* **2011**, 16, 135.
- [48] Z. R. Guo, Y. Wan, M. Wang, L. N. Xu, X. Lu, G. Yang, K. Fang, N. Gu, *Colloids Surf., A* **2012**, 414, 492.
- [49] J. W. Wu, W. F. Jia, W. S. Lu, L. Jiang, *ACS Appl. Mater. Interfaces* **2012**, 4, 6560.
- [50] Q. Li, R. B. Jiang, T. Ming, C. H. Fang, J. F. Wang, *Nanoscale* **2012**, 4, 7070.
- [51] W. Q. Zhang, H. Y. J. Goh, S. Firdoz, X. M. Lu, *Chem. Eur. J.* **2013**, 19, 12732.
- [52] S. Gómez-Graña, B. Goris, T. Altantzis, C. Fernández-López, E. Carbó-Argibay, A. Guerrero-Martínez, N. Almora-Barrios, N. López, I. Pastoriza-Santos, J. Pérez-Juste, S. Bals, G. Van Tendeloo, L. M. Liz-Marzán, *J. Phys. Chem. Lett.* **2013**, 4, 2209.
- [53] K. Park, H. Koerner, R. A. Vaia, *Nano Lett.* **2010**, 10, 1433.
- [54] B. P. Khanal, E. R. Zubarev, *J. Am. Chem. Soc.* **2008**, 130, 12634.
- [55] N. R. Jana, *Chem. Commun.* **2003**, 1950.
- [56] N. Verellen, F. López-Tejiera, R. Paniagua-Domínguez, D. Vercruysse, D. Denkova, L. Lagae, P. Van Dorpe, V. V. Moshchalkov, J. A. Sánchez-Gil, *Nano Lett.* **2014**, 14, 2322.
- [57] Y. G. Sun, B. Gates, B. Mayers, Y. N. Xia, *Nano Lett.* **2002**, 2, 165.
- [58] R. B. Jiang, H. J. Chen, L. Shao, Q. Li, J. F. Wang, *Adv. Mater.* **2012**, 24, OP200.
- [59] H. Dittlbacher, A. Hohenau, D. Wagner, U. Kreibitz, M. Rogers, F. Hofer, F. R. Aussenegg, J. R. Krenn, *Phys. Rev. Lett.* **2005**, 95, 257403.
- [60] C. J. Orendorff, C. J. Murphy, *J. Phys. Chem. B* **2006**, 110, 3990.

- [61] C. Sönnichsen, T. Franzl, T. Wilk, G. von Plessen, J. Feldmann, O. Wilson, P. Mulvaney, *Phys. Rev. Lett.* **2002**, *88*, 077402.
- [62] W. R. Zipfel, R. M. Williams, W. W. Webb, *Nat. Biotechnol.* **2003**, *21*, 1369.
- [63] C. E. Olson, M. J. R. Previte, J. T. Fourkas, *Nat. Mater.* **2002**, *1*, 225.
- [64] W. H. Zhou, S. M. Kuebler, K. L. Braun, T. Y. Yu, J. K. Cammack, C. K. Ober, J. W. Perry, S. R. Marder, *Science* **2002**, *296*, 1106.
- [65] K. Imura, T. Nagahara, H. Okamoto, *J. Am. Chem. Soc.* **2004**, *126*, 12730.
- [66] A. Bouhelier, R. Bachelot, G. Lerondel, S. Kostcheev, P. Royer, G. P. Wiederrecht, *Phys. Rev. Lett.* **2005**, *95*, 267405.
- [67] H. F. Wang, T. B. Huff, D. A. Zweifel, W. He, P. S. Low, A. Wei, J.-X. Cheng, *Proc. Natl. Acad. Sci. U. S. A.* **2005**, *102*, 15752.
- [68] N. J. Durr, T. Larson, D. K. Smith, B. A. Korgel, K. Sokolov, A. Ben-Yakar, *Nano Lett.* **2007**, *7*, 941.
- [69] T. T. Zhao, X. Q. Shen, L. Li, Z. P. Guan, N. Y. Gao, P. Y. Yuan, S. Q. Yao, Q.-H. Xu, G. Q. Xu, *Nanoscale* **2012**, *4*, 7712.
- [70] K. A. Willets, R. P. Van Duyne, *Annu. Rev. Phys. Chem.* **2007**, *58*, 267.
- [71] Y. Fang, N.-H. Seong, D. D. Dlott, *Science* **2008**, *321*, 388.
- [72] L. Zhao, T. Ming, G. S. Li, C. J. Chen, J. F. Wang, J. C. Yu, *Small* **2010**, *6*, 1880.
- [73] L. Shao, Q. F. Ruan, R. B. Jiang, J. F. Wang, *Small* **2014**, *10*, 802.